

Look Inside for More: Internal Spatial Modality Perception for 3D Anomaly Detection

Hanzhe Liang^{1,2}, Guoyang Xie⁴, Chengbin Hou⁵, Bingshu Wang⁶, Can Gao^{1*}, Jinbao Wang^{3,7*}

¹ College of Computer Science and Software Engineering, Shenzhen University, Shenzhen, China.

² Shenzhen Audencia Financial Technology Institute, Shenzhen University, Shenzhen, China.

³ National Engineering Laboratory for Big Data System Computing Technology, Shenzhen University, Shenzhen, China.

⁴ Department of Intelligent Manufacturing, CATL, Ningde, China.

⁵ School of Computing and Artificial Intelligence, Fuyao University of Science and Technology, Fuzhou, China.

⁶ School of Software, Northwestern Polytechnical University, Xi'an, China.

⁷ Guangdong Provincial Key Laboratory of Intelligent Information Processing, Shenzhen, China.

2023362051@email.szu.edu.cn, guoyang.xie@ieee.org, chengbin.hou10@foxmail.com, wangbingshu@nwpu.edu.cn, davidgao@szu.edu.cn, wangjb@szu.edu.cn

Abstract

3D anomaly detection has recently become a significant focus in computer vision. Several advanced methods have achieved satisfying anomaly detection performance. However, they typically concentrate on the external structure of 3D samples and struggle to leverage the internal information embedded within samples. Inspired by the basic intuition of why not look inside for more, we introduce a straightforward method named Internal Spatial Modality Perception (ISMP) to explore the feature representation from internal views fully. Specifically, our proposed ISMP consists of a critical perception module, Spatial Insight Engine (SIE), which abstracts complex internal information of point clouds into essential global features. Besides, to better align structural information with point data, we propose an enhanced key point feature extraction module for amplifying spatial structure feature representation. Simultaneously, a novel feature filtering module is incorporated to reduce noise and redundant features for further aligning precise spatial structure. Extensive experiments validate the effectiveness of our proposed method, achieving object-level and pixel-level AUROC improvements of 4.2% and 13.1%, respectively, on the Real3D-AD benchmarks. Note that the strong generalization ability of SIE has been theoretically proven and is verified in both classification and segmentation tasks.

Introduction

3D anomaly detection (AD) plays a crucial role in industrial and medical applications by identifying abnormalities in complex structures. Traditional methods, such as BTF (Horwitz and Hoshen 2022), primarily focus on single-sample analysis, while recent deep learning-based approaches have improved detection by incorporating cross-sample information. However, these methods often rely on intuitive feature extraction, which may overlook deeper anomalies. Researchers are exploring different strategies to uncover finer

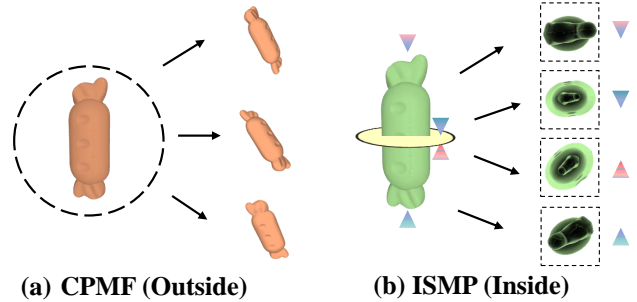


Figure 1: Visualization of internal and external perception. Compared with external view (CPMF), our method (ISMP) projects from the internal view, better capturing the different-shaped protrusions in the 3D structure.

details, with some emphasizing 3D data alone and others integrating multi-modal approaches.

The methods centered on 3D structures emphasize the unique feature representation of the structure. For example, (Bergmann and Sattlegger 2022) used geometric descriptors with a teacher-student model to achieve promising results, while (Rudolph et al. 2022) introduced asymmetric networks to enhance discrimination further. Additionally, (Li et al. 2023) focused on improving local feature representations, and (Kruse et al. 2024) proposed leveraging pose information for better anomaly detection across different viewpoints. Despite these advancements, many methods start from an intuitive structure, potentially leading to incomplete information coverage. On the other hand, multi-modal methods provide richer feature representations by integrating different data modalities. For instance, combining RGB 2D and 3D data (Wang et al. 2023) or using independent evaluations of both (Chu et al. 2023) has enhanced detection capabilities. (Zavrtanik, Kristan, and Skočaj 2023) leveraged depth and RGB information to identify anomalies better, while (Bhunja, Li, and Bilen 2024) advanced 2D-3D detection by constructing a query image database. However,

*Corresponding authors.

challenges such as feature alignment losses and increased sensor data demands persist. To address these issues, (Cao, Xu, and Shen 2023) introduced a pseudo-modal approach that projects 3D data into 2D images for supplementary information. While this method offers a more comprehensive representation, it still neglects internal structural details, resulting in incomplete feature coverage and reducing detection performance.

Could we shift focus toward internal information for more comprehensive anomaly detection? To tackle the challenges of insufficient internal information utilization and difficulties in aligning data across different modalities in anomaly detection using pseudo-modalities, we propose a novel method centered on internal spatial pseudo-modalities. Figure 1 shows the comparison between our method’s internal perception and counterparts that obtain global features from the outside. Our approach effectively captures the internal characteristics of 3D structures, even in low-sample environments, by leveraging the internal spatial features of point clouds. It facilitates better interactions between internal structures and surface regions, creating a complementary relationship between internal and external information. The core of our method, the Internal Spatial Modality Perception (ISMP) framework, includes a Spatial Insight Engine (SIE) that captures global features, an enhanced feature extraction module for local details, and a feature filtering module to suppress redundant data. Together, these components significantly improve anomaly detection accuracy. Note that our SIE indicates strong generalization capabilities, making it suitable for a broader range of point cloud tasks.

The main contributions of this paper are summarized as follows:

- To our best of knowledge, we are the first to focus on the internal structure of point clouds, thereby improving the extraction of internal structural features.
- A new Internal Spatial Modality Perception (ISMP) module and an Enhanced feature extraction combined with a feature filtering module, are designed to improve the perception and alignment of local features of key points.
- The feasibility of Spatial Insight Engine (SIE) is explored in tasks of classification and segmentation, emphasizing the strong generalization ability of the internal spatial pseudo-modality.
- Numerous experiments demonstrate the superiority of ISMP, surpassing the state-of-the-art methods on Real3D-AD with 13.1% and 4.1% improvements in P-AUROC and O-AUROC.

2D Anomaly Detection

2D image anomaly detection, a widely studied area, typically involves two main components: feature extraction and feature modeling. Feature extraction aims to derive discriminative features that distinguish normal from anomalous data. In contrast, feature modeling captures the distribution of normal features and detects deviations when anomalies are present. Early methods focused on learning features from scratch, such as through autoencoders and inpainting tasks,

with notable approaches like RIAD, and DRAEM making significant strides in this area (Bergmann et al. 2019; Park et al. 2023; Zavrtnik, Kristan, and Skočaj 2021). However, recent advancements have demonstrated the effectiveness of using pre-trained networks for anomaly detection. Techniques like knowledge distillation, as employed in ST and AST, align features between teacher and student networks to detect anomalies, addressing issues like overgeneralization (Yamada and Hotta 2022; Rudolph et al. 2022). Further innovations include normalizing flow and memory bank techniques to model normal feature distributions more effectively (Gudovskiy, Ishizaka, and Kozuka 2021). These developments improve 2D anomaly detection and lay the groundwork for extending these methods to 3D and multi-modal detection, driving further progress in the field.

3D Anomaly Detection

3D anomaly detection, such as point cloud AD, is crucial in domains like autonomous vehicular navigation and industrial inspections (Solaas, Tuptuk, and Mariconti 2024; Cui et al. 2022). Deep learning-based anomaly detection leverages neural networks to capture intricate point cloud structures. Techniques like PatchCore and its successors have made significant strides by learning point cloud representations directly from raw data (Tu et al. 2024; Roth et al. 2022). These methods emphasize efficient feature extraction and fusion, crucial for effective anomaly detection. Advanced approaches like PointNet++ and Point Transformer improve feature extraction by incorporating hierarchical and attention mechanisms (Wu et al. 2024; Zhao et al. 2021; Qi et al. 2017b). Additionally, techniques like PointMAE and PointMLP further enhance local feature extraction and fusion (Pang et al. 2022; Ma et al. 2022). Mathematical strategies, including coupled Laplacian eigenmaps and locality-sensitive methods, also contribute to more nuanced point cloud representations, enhancing 3D anomaly detection (Bastico et al. 2024; Chen et al. 2023; Bergmann and Sattlegger 2022). Finally, point cloud coordinates, exemplified by methods like FPFH, provide essential feature information for anomaly detection (Rusu, Blodow, and Beetz 2009).

In parallel, pseudo-modality techniques, which simulate modality data through a single modality or fabricated features, aim to enhance feature representation by combining diverse types of information. Recent advancements have addressed some of these shortcomings. For instance, methods discussed in (Cao, Xu, and Shen 2023) have focused on leveraging pseudo-modal features from multiple viewpoints. Building on this, (Bhunia, Li, and Bilen 2024) further improves the capture of texture information by aligning and transposing 2D features onto 3D point clouds using extensive 2D image databases for referencing. However, despite these advancements, these methodologies commonly need to work on fully exploiting the intricate internal structure of point clouds. They predominantly focus on extrinsic information while overlooking essential internal complexities. Consequently, this oversight limits their effectiveness in fully capturing the nuanced internal features necessary for comprehensive anomaly detection.

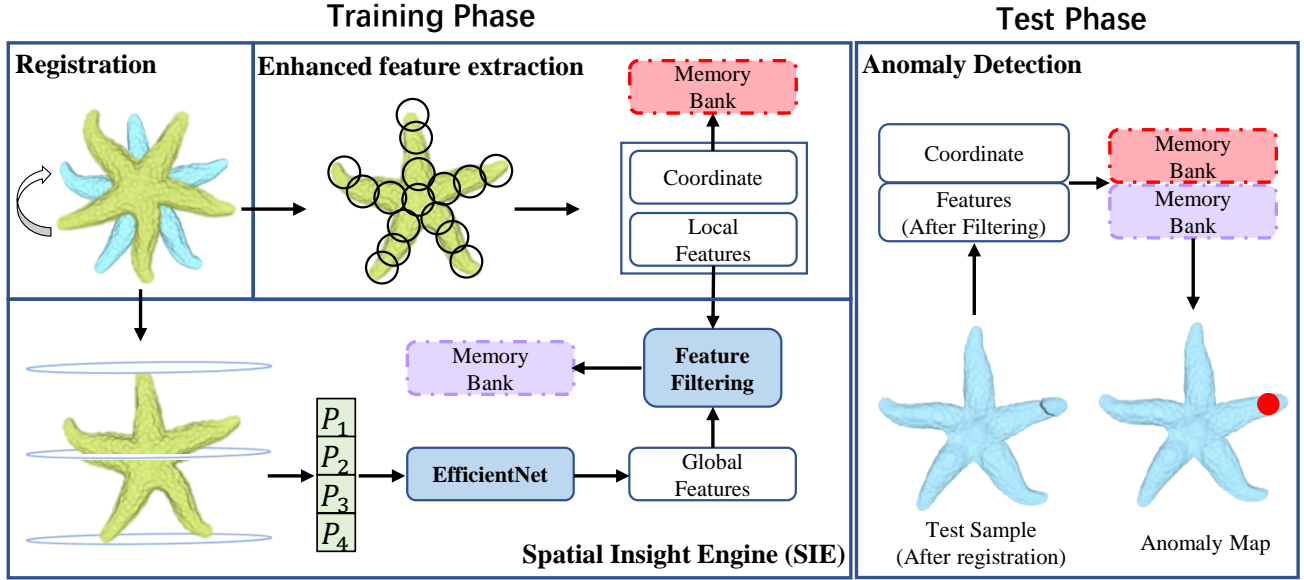


Figure 2: Overview of our method. We start by matching the point cloud according to RANSAC (Li, Hu, and Ai 2021). During the training phase, we create feature and coordinate memory banks, using enhanced feature extraction to capture local information and constructing a local feature matrix. We extract global features using the SIE and align them with the local ones. P_1 , P_2 , P_3 , and P_4 are the four projection slices extracted respectively. Then, we employ a feature filtering module to suppress redundant information, resulting in the final feature matrix. In the inference phase, we obtain the final feature matrix and compute the nearest neighbors in the memory bank. Finally, we input the coordinates into the coordinate memory bank to find the closest regular sample coordinates, calculating the final score of the sample points based on both memory banks.

Method

Spatial Insight Engine

Figure 2 provides an overview of our method. We have developed a robust model (SIE) that seamlessly converts 3D point cloud structures into 2D pseudo-modal data using advanced four projection slices (P_1 , P_2 , P_3 , P_4), as shown in Figure 2. These meticulously designed slices conduct thorough top-down and bottom-up analyses at the point cloud’s top, middle, and bottom. More notably, the middle slice (P_2 , P_3) expertly partitions the point cloud into two parts, working synergistically with the other slice to extract comprehensive features from both segments. The visualization of the projection slices is shown in Figure 3.

Taking the upper part of the point cloud as an example, we explain why extracting features from the SIE can capture more information and effectively detect anomalies.

Information Capturing Analysis. The amount of information can be defined as:

$$\mathbf{P} = \{\mathbf{p}_i = (x_i, y_i, z_i) \mid i \in \{1, 2, \dots, N\}\}, \quad (1)$$

where \mathbf{P} is the set of points, \mathbf{p}_i represents individual points with coordinates (x_i, y_i, z_i) , and N is the total number of points. And the midpoint z_{mid} is defined as:

$$z_{mid} = \frac{z_{\min} + z_{\max}}{2}, \quad (2)$$

where z_{mid} is along the z-axis, z_{\min} and z_{\max} are the mini-

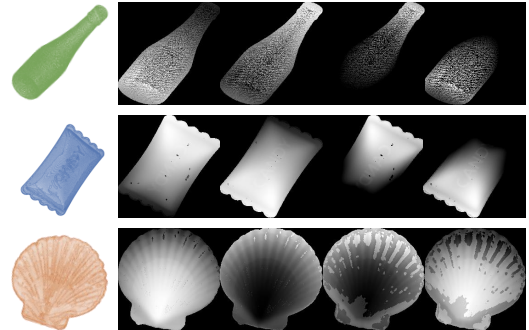


Figure 3: Visualization of projection slices. The images are the original image, P_1 , P_2 , P_3 , and P_4 , respectively.

mum and maximum z-coordinates, respectively.

$$I_{top} = \sum_{i=1}^N (z_{\max} - z_i), \quad (3)$$

where I_{top} is the top information, z_i is the z-coordinate of point i . Based on our SIE calculation, we have the global information:

$$I_{global} = \sum_{i=1}^N [(z_{\max} - z_i) + \max(0, z_i - z_{mid})]. \quad (4)$$

After rewriting, we have:

$$I_{global} = I_{top} + \sum_{i:z_i \geq z_{mid}} (z_i - z_{mid}) \geq I_{top}. \quad (5)$$

Therefore, we observe that I_{global} has more information than I_{top} , which is standard external projection manner. The same goes for the lower half of the point cloud. In this way, the final information obtained by the point cloud will be more reliable than if only external modes are used.

Anomaly Detection. Deep information contains important exception information (Liu et al. 2024). An anomaly can be detected when the discrepancy between the depth values from the two views significantly deviates from the expected range for normal points. That is

$$|\Delta D(\mathbf{p}_i) - \mu_{\Delta D}| > k\sigma_{\Delta D}, \quad (6)$$

where $\Delta D(\mathbf{p}_i)$ is the discrepancy between top-down and middle-up depth values. Besides, $\mu_{\Delta D}$ and $\sigma_{\Delta D}$ are the mean and standard deviation of ΔD for average points respectively, with k as a threshold constant.

Given these constraints, the SIE enhances global information by observing from an internal perspective, significantly improving anomaly detection compared to relying solely on external spatial capture.

Enhanced Feature Extraction

Following the instructions in the relevant work, we utilize Farthest Point Sampling (FPS) to obtain a set of center points, treating the k-nearest neighbors around each center point as a patch for processing (Qi et al. 2017b). Following the PointMAE method, we derive the patch features (Pang et al. 2022). Then, we perform feature extraction on the center points according to FPFH, obtaining more comprehensive features (Rusu, Blodow, and Beetz 2009). We have:

$$\text{FPS}(X) = \{x_i\}_{i=1}^m, \quad (7)$$

where X represents the original point cloud and $\{x_i\}$ are the sampled center points.

For each center point x_i , we define its patch P_i as:

$$P_i = \{x \in X \mid \|x - x_i\| \leq r\}, \quad (8)$$

where r is the radius defining the neighborhood of x_i . Using PointMAE, we extract features for each patch (P_i). Then, we use Fast Point Feature Histograms (FPFH) to further enhance feature representation for each center point.

Feature Filtering Module

The information extracted from the point cloud is often too miscellaneous, and we usually need to perform noise reduction and other processing on the direct information extracted from the point cloud (Cao et al. 2023). The Laplacian transform (Kipf and Welling 2017) is widely used in feature filtering to enhance the quality of features by removing noise and redundant information. It helps in achieving better feature representation and alignment, especially in high-dimensional data such as point clouds (Shao et al. 2017; Ghogh et al. 2022). By applying the Laplacian transform,

models can achieve smoother and more accurate feature extraction, which is crucial for tasks requiring precise geometric representations.

The Laplacian matrix L is denoted as:

$$L = D - A, \quad (9)$$

where D is the degree matrix and A is the adjacency matrix of the graph. This transformation allows for the enhancement of the overall feature quality by smoothing out irregularities and focusing on the intrinsic geometric structure (Zeng et al. 2019).

To achieve better alignment of features from SIE and enhancements, we develop a controllable feature filtering module using the Laplace transform to enhance geometric features in point clouds. This method is outlined in pseudo-code and relies on specific parameters. The process can be summarized by the following equation:

$$\text{Fill}(X|\alpha, \beta, \gamma) = X_{\text{enhanced}}, \quad (10)$$

where α , β , and γ are the parameters that control the influence of the enhanced Laplacian, the decay rate of the weight matrix, and the contribution of the anomaly metric, respectively. X is the original feature matrix, and X_{enhanced} is the resulting enhanced feature matrix. The overall implementation of this module is shown in Algorithm 1.

Algorithm 1: Feature Filtering Module

```

1: procedure FILTERING( $X, \alpha, \beta, \gamma$ )
2:    $n \leftarrow X.shape()$ 
3:    $A \leftarrow \mathbf{1}_{n \times n} - \mathbf{I}_n$ 
4:    $D \leftarrow \text{diag}(A.sum(\text{dim} = 1))$ 
5:    $M \leftarrow \text{cdist}(X, X, p = 2)$ 
6:    $W \leftarrow \exp(-\beta \cdot M)$   $\triangleright$  Control similarity weighting
7:    $A' \leftarrow A \cdot W$ 
8:    $D' \leftarrow \text{diag}(A'.sum(\text{dim} = 1))$ 
9:    $D'^{-0.5} \leftarrow \text{diag}(D'.diag()^{-0.5})$ 
10:   $L'_{\text{sym}} \leftarrow \mathbf{I}_n - D'^{-0.5} \cdot A' \cdot D'^{-0.5}$ 
11:   $mask \leftarrow A == 0$ 
12:   $masked\_M \leftarrow M.masked\_fill(mask, \text{nan})$ 
13:   $E \leftarrow \text{nanmean}(masked\_M, \text{dim} = 1)$ 
14:   $L_{\text{final}} \leftarrow L'_{\text{sym}} + \gamma \cdot \text{diag}(E)$   $\triangleright$  Adjust Laplacian matrix
15:   $X_{\text{enhanced}} \leftarrow (\mathbf{I}_n + \alpha \cdot L_{\text{final}}) \cdot X$   $\triangleright$  Enhance features
16:   $X_{\text{max}} \leftarrow X.max()$ 
17:   $X_{\text{enhanced}} \leftarrow X_{\text{enhanced}} \cdot (X_{\text{max}}/X_{\text{enhanced}}.max())$ 
18:  return  $X_{\text{enhanced}}$ 
19: end procedure

```

Anomaly Score Calculation

We utilize the feature memory bank \mathcal{M}^C and the coordinate memory bank \mathcal{M}^F to compute anomaly scores. Here, we illustrate the scoring process using the \mathcal{M}^F memory bank as an example. We find the nearest neighbor in the \mathcal{M}^F for the test object's point-level feature $\mathcal{P}(m^{\text{test}})$. The nearest neighbor search method (Liu et al. 2023) is denoted as:

$$m^{\text{test},*} = \arg \max_{m^{\text{test}} \in \mathcal{P}(x^{\text{test}})} \min_{m' \in \mathcal{M}^F} \|m^{\text{test}} - m'\|_2, \quad (11)$$

$$m_*^F = \arg \min_{m' \in \mathcal{M}^F} \|m^{\text{test}} - m'\|_2.$$

(a) O-AUROC (\uparrow)													
Method	Airplane	Car	Candy	Chicken	Diamond	Duck	Fish	Gemstone	Seahorse	Shell	Starfish	Toffees	Mean
BTF(Raw)	0.730	0.647	0.539	0.789	0.707	0.691	0.602	0.686	0.596	0.396	0.530	0.703	0.635
BTF(FPFH)	0.520	0.560	0.630	0.432	0.545	0.784	0.549	0.648	0.779	0.754	0.575	0.462	0.603
M3DM	0.434	0.541	0.552	0.683	0.602	0.433	0.540	0.644	0.495	0.694	0.551	0.450	0.552
PatchCore(FPFH)	0.882	0.590	0.541	0.837	0.574	0.546	0.675	0.370	0.505	0.589	0.441	0.565	0.593
PatchCore(PointMAE)	0.726	0.498	0.663	0.827	0.783	0.489	0.630	0.374	0.539	0.501	0.519	0.585	0.594
CPMF	0.701	0.551	0.552	0.504	0.523	0.582	0.558	0.589	0.729	0.653	0.700	0.390	0.586
RegAD	0.716	0.697	0.685	0.852	0.900	0.584	0.915	0.417	0.762	0.583	0.506	0.827	0.704
IMRNet	0.762	0.711	0.755	0.780	0.905	0.517	0.880	0.674	0.604	0.665	0.674	0.774	0.725
ISMP(Ours)	0.858	0.731	0.852	0.714	0.948	0.712	0.945	0.468	0.729	0.623	0.660	0.842	0.767

(b) P-AUROC (\uparrow)													
Method	Airplane	Car	Candy	Chicken	Diamond	Duck	Fish	Gemstone	Seahorse	Shell	Starfish	Toffees	Mean
BTF(Raw)	0.564	0.647	0.735	0.609	0.563	0.601	0.514	0.597	0.520	0.489	0.392	0.623	0.571
BTF(FPFH)	0.738	0.708	0.864	0.735	0.882	0.875	0.709	0.891	0.512	0.571	0.501	0.815	0.733
M3DM	0.547	0.602	0.679	0.678	0.608	0.667	0.606	0.674	0.560	0.738	0.532	0.682	0.631
PatchCore(FPFH)	0.562	0.754	0.780	0.429	0.828	0.264	0.829	0.910	0.739	0.739	0.606	0.747	0.682
PatchCore(PointMAE)	0.569	0.609	0.627	0.729	0.718	0.528	0.717	0.444	0.633	0.709	0.580	0.580	0.620
RegAD	0.631	0.718	0.724	0.676	0.835	0.503	0.826	0.545	0.817	0.811	0.617	0.759	0.705
ISMP(Ours)	0.753	0.836	0.907	0.798	0.926	0.876	0.886	0.857	0.813	0.839	0.641	0.895	0.836

Table 1: The experimental results of (a) O-AUROC (\uparrow) and (b) P-AUROC (\uparrow) for anomaly detection across 12 categories of Real3D-AD. The best and the second-best results are highlighted in red and blue, respectively. Our model achieved the best average performance across the 12 categories for both metrics.

Calculate the nearest neighbor distance as the local feature anomaly score s_*^F :

$$s_*^F = \|m^{\text{test},*} - m_*^F\|_2. \quad (12)$$

The anomaly score is adjusted using a re-weighting method (Liu and Tao 2016), which is denoted as:

$$s^F = \left(1 - \frac{\exp\|m^{\text{test},*} - m_*^F\|_2}{\sum_{m \in N_3(m^*)} \exp\|m^{\text{test},*} - m\|_2}\right) s_*^F. \quad (13)$$

Here, $N_3(m^*)$ represents the 3 nearest features in the \mathcal{M}^F . Perform similar calculations using the \mathcal{M}^C to obtain the coordinate anomaly score s^C .

$$s = \frac{s^F + s^C}{2}. \quad (14)$$

Compute the overall anomaly score for each point cloud s by averaging the s^F and s^C using Equ. (14).

Experiments

In this section, we firstly evaluated the effectiveness of ISMP in the anomaly detection task and secondly supplemented the assessment with the generalization ability of SIE across multiple tasks.

Implementation

Datasets. We conducted comparative experiments on two mainstreaming datasets, namely Real3D-AD and Anomaly-ShapeNet. (1) The Real3D-AD dataset (Liu et al. 2023) is a high-resolution, large-scale anomaly dataset containing 1,254 samples across 12 categories. The training set for each category includes four normal samples, while the test set for each category contains both normal samples and anomalous samples with various defects. (2) The Anomaly-ShapeNet

dataset (Li et al. 2023) provides 40 categories, containing over 1,600 positive and negative samples. The training set for each category includes four normal samples, while the test set for each category contains both normal samples and anomalous samples with various defects.

Baselines. We selected BTF (Horwitz and Hoshen 2022), M3DM (Wang et al. 2023), PatchCore (Roth et al. 2022), CPMF (Cao, Xu, and Shen 2023), RegAD (Liu et al. 2023), and IMRNet (Li et al. 2023) for comparison. Note that BTF(FPFH) denotes that we incorporate fast point feature histogram (Rusu, Blodow, and Beetz 2009). The results of these methods are obtained through publicly available code or referenced papers.

Evaluation Metrics. For the anomaly detection task, we use P-AUROC (\uparrow) to evaluate pixel-level anomaly localization capability and O-AUROC (\uparrow) to evaluate object-level anomaly detection capability. Higher values for both metrics indicate a more robust anomaly detection capability.

Experimental Details. The experiments are conducted on a machine equipped with an RTX 3090 (24GB) GPU. For ISMP, we used the pre-trained weights of the PointMAE and EfficientNet (Tan and Le 2020) models to complete our experiments. Our parameter settings for ISMP followed those of RegAD (Liu et al. 2023), with α set to 0.2, β set to 0.2, and γ set to 0.001.

Main Results

Comparisons on Real3D-AD. The quantitative comparisons of ISMP with competing models are presented in Table 1. We observed that other models exhibit biases in high-precision anomaly localization tasks, making accurate localization challenging. Our method achieved O-AUROC and P-AUROC scores of 0.767 and 0.836, respectively, significantly improving state-of-the-art (SOTA) methods.

P-AUROC (\uparrow)														
Method	cap0	cap3	helmet3	cup0	bow14	vase3	headset1	eraser0	vase8	cap4	vase2	vase4	helmet0	bucket1
BTF(Raw)	0.524	0.687	0.700	0.632	0.563	0.602	0.475	0.637	0.550	0.469	0.403	0.613	0.504	0.686
BTF(FPFH)	0.730	0.658	0.724	0.790	0.679	0.699	0.591	0.719	0.662	0.524	0.646	0.710	0.575	0.633
M3DM	0.531	0.605	0.655	0.715	0.624	0.658	0.585	0.710	0.551	0.718	0.737	0.655	0.599	0.699
Patchcore(FPFH)	0.472	0.653	0.737	0.655	0.720	0.430	0.464	0.810	0.575	0.595	0.721	0.505	0.548	0.571
Patchcore(PointMAE)	0.544	0.488	0.615	0.510	0.501	0.465	0.423	0.378	0.364	0.725	0.742	0.523	0.580	0.754
CPMF	0.601	0.551	0.520	0.497	0.683	0.582	0.458	0.689	0.529	0.553	0.582	0.514	0.555	0.601
RegAD	0.632	0.718	0.620	0.685	0.800	0.511	0.626	0.755	0.811	0.815	0.405	0.755	0.600	0.725
IMRNet	0.715	0.706	0.663	0.643	0.576	0.401	0.476	0.548	0.635	0.753	0.614	0.524	0.598	0.774
ISMP(Ours)	0.865	0.734	0.722	0.869	0.740	0.762	0.702	0.706	0.851	0.753	0.733	0.545	0.683	0.672

Method	bottle3	vase0	bottle0	tap1	bow10	bucket0	vase5	vase1	vase9	ashtray0	bottle1	tap0	phone	cup1
BTF(Raw)	0.720	0.618	0.551	0.564	0.524	0.617	0.585	0.549	0.564	0.512	0.491	0.527	0.583	0.561
BTF(FPFH)	0.622	0.642	0.641	0.596	0.710	0.401	0.429	0.619	0.568	0.624	0.549	0.568	0.675	0.619
M3DM	0.532	0.608	0.663	0.712	0.658	0.698	0.642	0.602	0.663	0.577	0.637	0.654	0.358	0.556
Patchcore(FPFH)	0.512	0.655	0.654	0.768	0.524	0.459	0.447	0.453	0.663	0.597	0.687	0.733	0.488	0.596
Patchcore(PointMAE)	0.653	0.677	0.553	0.541	0.527	0.586	0.572	0.551	0.423	0.495	0.606	0.858	0.886	0.856
CPMF	0.435	0.458	0.521	0.657	0.745	0.486	0.651	0.486	0.545	0.615	0.571	0.458	0.545	0.509
RegAD	0.525	0.548	0.888	0.741	0.775	0.619	0.624	0.602	0.694	0.698	0.696	0.589	0.599	0.698
IMRNet	0.641	0.535	0.556	0.699	0.781	0.585	0.682	0.685	0.691	0.671	0.702	0.681	0.742	0.688
ISMP(Ours)	0.775	0.661	0.770	0.552	0.851	0.524	0.472	0.843	0.615	0.603	0.568	0.522	0.661	0.600

Method	vase7	helmet2	cap5	shelf0	bow15	bow13	helmet1	bow11	headset0	bag0	bow12	jar0	Mean
BTF(Raw)	0.578	0.605	0.373	0.464	0.517	0.685	0.449	0.464	0.578	0.430	0.426	0.423	0.550
BTF(FPFH)	0.540	0.643	0.586	0.619	0.699	0.690	0.749	0.768	0.620	0.746	0.518	0.427	0.628
M3DM	0.517	0.623	0.655	0.554	0.489	0.657	0.427	0.663	0.581	0.637	0.694	0.541	0.616
Patchcore(FPFH)	0.693	0.455	0.795	0.613	0.358	0.327	0.489	0.531	0.583	0.574	0.625	0.478	0.580
Patchcore(PointMAE)	0.651	0.651	0.545	0.543	0.562	0.581	0.562	0.524	0.575	0.674	0.515	0.487	0.577
CPMF	0.504	0.515	0.551	0.783	0.684	0.641	0.542	0.488	0.699	0.655	0.635	0.611	0.573
RegAD	0.881	0.825	0.467	0.688	0.691	0.654	0.624	0.645	0.580	0.715	0.593	0.599	0.668
IMRNet	0.593	0.644	0.742	0.605	0.715	0.599	0.604	0.705	0.615	0.668	0.684	0.765	0.650
ISMP(Ours)	0.701	0.844	0.678	0.687	0.534	0.773	0.622	0.546	0.580	0.747	0.736	0.823	0.691

Table 2: The experimental results of P-AUROC (\uparrow) for anomaly detection of 40 categories of Anomaly-ShapeNet. The best and the second-best results are highlighted in red and blue, respectively. Our model achieved better performance in pixel-level anomaly detection.

Comparisons on Anomaly-ShapeNet. In Table 2, we quantitatively analyze the pixel-level anomaly detection results on the Anomaly-ShapeNet dataset. Due to the diversity of the training set, Anomaly-ShapeNet presents challenges for better utilization of features. Our method achieved a P-AUROC score of 0.691, outperforming previous methods.

Ablation Study

Evaluation of the ISMP Efficiency. We evaluated each module’s effectiveness on Real3D-AD, as summarized in Table 3. The worst performance occurred with only coordinates and PointMAE features, emphasizing the need for improved local coordinate representation. Incorporating FPFH around sampled points increased P-AUROC by 18.9%, and further optimization with a feature filtering module added another 1.8%. Without global features, O-AUROC stayed at 65.6%, but introducing internal spatial modality features raised it by 11.1%. Notably, using only the two outer projection slices, omitting the internal slice, produced the second-best results, showing internal features are more reliable. These findings confirm our model’s optimal composition.

Evaluation of the ISMP Effectiveness. Our model achieved outstanding performance but grappled with inference efficiency challenges linked to incorporating extra modality information, as evidenced in Table 4. The ISMP lacks sufficient training and reasoning speed compared to its competitors.

Method	I-AUROC (\uparrow)	P-AUROC (\uparrow)
ISMP	0.767	0.836
ISMP _{w/o I}	0.656	0.827
ISMP _{w/o I&F}	0.623	0.809
ISMP _{w/o I,F&E}	0.594	0.620
ISMP _O	0.717	0.812

Table 3: Ablation study results. I and F represent SIE and the filter module respectively. E stands for enhanced feature extraction. O stands for using only the external projection and eliminating the internal projection.

Analysis of the Feature Filtering Module. The mean and variance of feature matrices play a crucial role in anomaly detection, as more concentrated feature distributions are beneficial for detecting anomalies (Wang et al. 2023). To further investigate the impact of the feature filtering module on feature matrices under different parameter settings, we present the effects of various parameters on the feature matrices in Figure 4. The variance of the feature matrix has a greater impact on distinguishing between abnormal and normal features than the mean. Specifically, controlling the variance in the feature matrix is crucial for better feature distinction. Notably, features from PointMAE resemble a standard normal distribution after normalization.

Method	Training	Test
RegAD	5.52	7.71
M3DM	4.50	6.43
ISMP (Ours)	2.78	4.37

Table 4: The average training and test time in terms of FPS (\uparrow , per sample) for models evaluated on the *seahorse* class.

We randomly selected one thousand feature matrices conforming to this distribution for feature filtering and analyzed their effects on the mean and variance. In practice, we conservatively chose the parameters labeled in the diagram. Our proposed feature filtering module ultimately exhibits controllability over the features, resulting in improved feature representations.

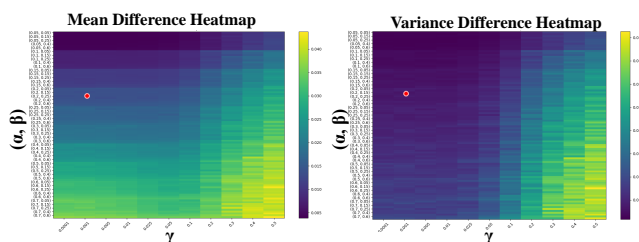


Figure 4: Heatmaps of the impact of parameters α , β , γ on mean and variance. The ordinate represents a combination of α and β , and the abscissa represents γ . The lighter the color of the block in the figure, the larger the difference before and after the transformation. The red marks in the figure are the parameters we selected.

Evaluation of SIE Generalization

To verify the effectiveness of SIE for the feature perception in 3D anomaly detection, we have designed two related tasks for point clouds, namely classification and segmentation. From the results, we can observe that SIE can provide more adequate information.

Datasets. (1) The ModelNet40 is a point cloud classification dataset containing forty categories (Wu et al. 2015). We use it to test the effect of SIE on classification tasks to prove generalization. (2) The ShapeNet-Part is a point cloud dataset commonly used for semantic segmentation. It includes ten categories of standard household items, with many 3D models corresponding to each category (Chang et al. 2015). We use it to test the impact of SIE on semantic segmentation tasks to prove generalization.

Evaluation Metrics. We use Accuracy (\uparrow) to evaluate the model’s capability for the point cloud classification task. For the segmentation task, we use Instance average Intersection over Union (IoU, \uparrow) to assess the model’s adaptability.

Baselines. To demonstrate its significant role in extracting global information from point clouds, we analyzed the effect of SIE in point cloud classification on ModelNet40, comparing it with Subvolume (Qi et al. 2016), MVCNN (Su et al. 2015), PointNet (Qi et al. 2017a), and PointNet++ (Qi et al.

2017b). Moreover, we tested the role of SIE in semantic segmentation on ShapeNet-Part, comparing it with Yi (Yi et al. 2016), PointNet, SSCNN (Yi et al. 2017) and PointNet++. The results of these methods are obtained through publicly available code or referenced papers. We employed the same PointNet++ settings as those used in (Qi et al. 2017b).

Comparison Results on ModelNet40. We used intra-space pseudo-modality as a crucial supplementary input for point cloud classification in PointNet++. As shown in Table 5, a simple feature injection is sufficient to enhance the performance of point cloud classification, since the intra-space pseudo-modality provides significant additional information for point clouds. It is proved that SIE has potential in point cloud classification tasks.

Method	Input	Accuracy (%)
Subvolume	vox	89.2
MVCNN	img	90.1
PointNet(vanilla)	pc	87.2
PointNet	pc	89.2
PointNet++	pc	90.7
PointNet++(SIE)	pc	91.1

Table 5: Shape classification results on ModelNet40.

Comparison Results on ShapeNet-Part. Using the global information from SIE as a supplement to features extracted by PointNet++ for part segmentation, we observed enhanced performance, as shown in Table 6. The results demonstrate SIE’s potential in aligning local and global information. Overall, ISMP excels in 3D anomaly detection, while SIE shows strong generalization and robustness, making it adaptable to other tasks.

Model	IoU (%)
Yi	81.4
PointNet	83.7
SSCNN	84.7
PointNet++	85.1
PointNet++(SIE)	85.4

Table 6: Segmentation results on ShapeNet-Part.

Conclusion

We propose a novel 3D AD method equipped with Internal Spatial Modality Perception (ISMP) to address the issue of underutilizing internal information in samples. Our approach consists of three modules, namely a novel perception module based on the Spatial Insight Engine (SIE), an enhanced feature extraction module, and a feature filtering module. The experimental results demonstrate the effectiveness of our proposed method. Besides, we verified the effectiveness of ISMP in the AD task and the generalization ability of SIE. **Limitation.** Given the limits of the test cost, we aim to improve the model’s inference speed in future work.

Acknowledgments

This work was supported by the National Natural Science Foundation of China (Grant Nos. 62206122, 62476171, 82261138629, 62302309), the Guangdong Basic and Applied Basic Research Foundation (No. 2024A1515011367), the Guangdong Provincial Key Laboratory (Grant No. 2023B1212060076), Shenzhen Municipal Science and Technology Innovation Council (Grant No. JCYJ20220531101412030), Tencent “Rhinoceros Birds” - Scientific Research Foundation for Young Teachers of Shenzhen University, and the Internal Fund of National Engineering Laboratory for Big Data System Computing Technology (Grant No. SZU-BDSC-IF2024-08).

References

- Bastico, M.; Decencière, E.; Corté, L.; Tillier, Y.; and Ryckelynck, D. 2024. Coupled Laplacian Eigenmaps for Locally-Aware 3D Rigid Point Cloud Matching. arXiv:2402.17372.
- Bergmann, P.; Löwe, S.; Fauser, M.; Sattlegger, D.; and Steger, C. 2019. Improving Unsupervised Defect Segmentation by Applying Structural Similarity to Autoencoders. In *Proceedings of the 14th International Joint Conference on Computer Vision, Imaging and Computer Graphics Theory and Applications*. SCITEPRESS - Science and Technology Publications.
- Bergmann, P.; and Sattlegger, D. 2022. Anomaly Detection in 3D Point Clouds using Deep Geometric Descriptors. arXiv:2202.11660.
- Bhunia, A.; Li, C.; and Bilen, H. 2024. Looking 3D: Anomaly Detection with 2D-3D Alignment. arXiv:2406.19393.
- Cao, X.; Xia, H.; Han, X.; Wang, Y.; Li, K.; and Su, L. 2023. PointJEM: Self-supervised Point Cloud Understanding for Reducing Feature Redundancy via Joint Entropy Maximization. arXiv:2312.03339.
- Cao, Y.; Xu, X.; and Shen, W. 2023. Complementary Pseudo Multimodal Feature for Point Cloud Anomaly Detection. arXiv:2303.13194.
- Chang, A. X.; Funkhouser, T.; Guibas, L.; Hanrahan, P.; Huang, Q.; Li, Z.; Savarese, S.; Savva, M.; Song, S.; Su, H.; Xiao, J.; Yi, L.; and Yu, F. 2015. ShapeNet: An Information-Rich 3D Model Repository. arXiv:1512.03012.
- Chen, X.; Shi, S.; Zhang, C.; Zhu, B.; Wang, Q.; Cheung, K. C.; See, S.; and Li, H. 2023. Trajectoryformer: 3d object tracking transformer with predictive trajectory hypotheses. In *Proceedings of the IEEE/CVF International Conference on Computer Vision*, 18527–18536.
- Chu, Y.-M.; Liu, C.; Hsieh, T.-I.; Chen, H.-T.; and Liu, T.-L. 2023. Shape-Guided Dual-Memory Learning for 3D Anomaly Detection. In Krause, A.; Brunskill, E.; Cho, K.; Engelhardt, B.; Sabato, S.; and Scarlett, J., eds., *Proceedings of the 40th International Conference on Machine Learning*, volume 202 of *Proceedings of Machine Learning Research*, 6185–6194. PMLR.
- Cui, Y.; Chen, R.; Chu, W.; Chen, L.; Tian, D.; Li, Y.; and Cao, D. 2022. Deep Learning for Image and Point Cloud Fusion in Autonomous Driving: A Review. *IEEE Transactions on Intelligent Transportation Systems*, 23(2): 722–739.
- Ghohogh, B.; Ghodsi, A.; Karray, F.; and Crowley, M. 2022. Laplacian-Based Dimensionality Reduction Including Spectral Clustering, Laplacian Eigenmap, Locality Preserving Projection, Graph Embedding, and Diffusion Map: Tutorial and Survey. arXiv:2106.02154.
- Gudovskiy, D.; Ishizaka, S.; and Kozuka, K. 2021. CFLOW-AD: Real-Time Unsupervised Anomaly Detection with Localization via Conditional Normalizing Flows. arXiv:2107.12571.
- Horwitz, E.; and Hoshen, Y. 2022. Back to the Feature: Classical 3D Features are (Almost) All You Need for 3D Anomaly Detection. arXiv:2203.05550.
- Kipf, T. N.; and Welling, M. 2017. Semi-Supervised Classification with Graph Convolutional Networks. arXiv:1609.02907.
- Kruse, M.; Rudolph, M.; Woiwode, D.; and Rosenhahn, B. 2024. SplatPose & Detect: Pose-Agnostic 3D Anomaly Detection. arXiv:2404.06832.
- Li, J.; Hu, Q.; and Ai, M. 2021. Point Cloud Registration Based on One-Point RANSAC and Scale-Annealing Bi-weight Estimation. *IEEE Transactions on Geoscience and Remote Sensing*, 59(11): 9716–9729.
- Li, W.; Xu, X.; Gu, Y.; Zheng, B.; Gao, S.; and Wu, Y. 2023. Towards Scalable 3D Anomaly Detection and Localization: A Benchmark via 3D Anomaly Synthesis and A Self-Supervised Learning Network. arXiv:2311.14897.
- Liu, J.; Xie, G.; Chen, R.; Li, X.; Wang, J.; Liu, Y.; Wang, C.; and Zheng, F. 2023. Real3D-AD: A Dataset of Point Cloud Anomaly Detection. arXiv:2309.13226.
- Liu, J.; Xie, G.; Wang, J.; Li, S.; Wang, C.; Zheng, F.; and Jin, Y. 2024. Deep Industrial Image Anomaly Detection: A Survey. *Machine Intelligence Research*, 21(1): 104–135.
- Liu, T.; and Tao, D. 2016. Classification with Noisy Labels by Importance Reweighting. *IEEE Transactions on Pattern Analysis and Machine Intelligence*, 38(3): 447–461.
- Ma, X.; Qin, C.; You, H.; Ran, H.; and Fu, Y. 2022. Rethinking Network Design and Local Geometry in Point Cloud: A Simple Residual MLP Framework. arXiv:2202.07123.
- Pang, Y.; Wang, W.; Tay, F. E. H.; Liu, W.; Tian, Y.; and Yuan, L. 2022. Masked Autoencoders for Point Cloud Self-supervised Learning. arXiv:2203.06604.
- Park, Y.; Kang, S.; Kim, M. J.; Lee, Y.; Kim, H. S.; and Yi, J. 2023. Excision And Recovery: Visual Defect Obfuscation Based Self-Supervised Anomaly Detection Strategy. arXiv:2310.04010.
- Qi, C. R.; Su, H.; Mo, K.; and Guibas, L. J. 2017a. PointNet: Deep Learning on Point Sets for 3D Classification and Segmentation. arXiv:1612.00593.
- Qi, C. R.; Su, H.; Niessner, M.; Dai, A.; Yan, M.; and Guibas, L. J. 2016. Volumetric and Multi-View CNNs for Object Classification on 3D Data. arXiv:1604.03265.
- Qi, C. R.; Yi, L.; Su, H.; and Guibas, L. J. 2017b. PointNet++: Deep Hierarchical Feature Learning on Point Sets in a Metric Space. arXiv:1706.02413.

- Roth, K.; Pemula, L.; Zepeda, J.; Schölkopf, B.; Brox, T.; and Gehler, P. 2022. Towards Total Recall in Industrial Anomaly Detection. arXiv:2106.08265.
- Rudolph, M.; Wehrbein, T.; Rosenhahn, B.; and Wandt, B. 2022. Asymmetric Student-Teacher Networks for Industrial Anomaly Detection. arXiv:2210.07829.
- Rusu, R. B.; Blodow, N.; and Beetz, M. 2009. Fast Point Feature Histograms (FPFH) for 3D registration. In *2009 IEEE International Conference on Robotics and Automation*, 3212–3217.
- Shao, Y.; Zhang, Z.; Li, Z.; Fan, K.; and Li, G. 2017. Attribute Compression of 3D Point Clouds Using Laplacian Sparsity Optimized Graph Transform. arXiv:1710.03532.
- Solaas, J. R. V.; Tuptuk, N.; and Mariconti, E. 2024. Systematic Review: Anomaly Detection in Connected and Autonomous Vehicles. arXiv:2405.02731.
- Su, H.; Maji, S.; Kalogerakis, E.; and Learned-Miller, E. 2015. Multi-view Convolutional Neural Networks for 3D Shape Recognition. In *2015 IEEE International Conference on Computer Vision (ICCV)*, 945–953.
- Tan, M.; and Le, Q. V. 2020. EfficientNet: Rethinking Model Scaling for Convolutional Neural Networks. arXiv:1905.11946.
- Tu, Y.; Zhang, B.; Liu, L.; Li, Y.; Chen, X.; Zhang, J.; Wang, Y.; Wang, C.; and Zhao, C. R. 2024. Self-supervised Feature Adaptation for 3D Industrial Anomaly Detection. arXiv:2401.03145.
- Wang, Y.; Peng, J.; Zhang, J.; Yi, R.; Wang, Y.; and Wang, C. 2023. Multimodal Industrial Anomaly Detection via Hybrid Fusion. arXiv:2303.00601.
- Wu, X.; Jiang, L.; Wang, P.-S.; Liu, Z.; Liu, X.; Qiao, Y.; Ouyang, W.; He, T.; and Zhao, H. 2024. Point Transformer V3: Simpler, Faster, Stronger. arXiv:2312.10035.
- Wu, Z.; Song, S.; Khosla, A.; Yu, F.; Zhang, L.; Tang, X.; and Xiao, J. 2015. 3D ShapeNets: A Deep Representation for Volumetric Shapes. arXiv:1406.5670.
- Yamada, S.; and Hotta, K. 2022. Reconstruction Student with Attention for Student-Teacher Pyramid Matching. arXiv:2111.15376.
- Yi, L.; Kim, V. G.; Ceylan, D.; Shen, I.-C.; Yan, M.; Su, H.; Lu, C.; Huang, Q.; Sheffer, A.; and Guibas, L. 2016. A scalable active framework for region annotation in 3D shape collections. *ACM Trans. Graph.*, 35(6).
- Yi, L.; Su, H.; Guo, X.; and Guibas, L. 2017. SyncSpec-CNN: Synchronized Spectral CNN for 3D Shape Segmentation. In *2017 IEEE Conference on Computer Vision and Pattern Recognition (CVPR)*, 6584–6592.
- Zavrtanik, V.; Kristan, M.; and Skočaj, D. 2021. DRAEM – A discriminatively trained reconstruction embedding for surface anomaly detection. arXiv:2108.07610.
- Zavrtanik, V.; Kristan, M.; and Skočaj, D. 2023. Cheating Depth: Enhancing 3D Surface Anomaly Detection via Depth Simulation. arXiv:2311.01117.
- Zeng, J.; Cheung, G.; Ng, M.; Pang, J.; and Yang, C. 2019. 3D Point Cloud Denoising using Graph Laplacian Regularization of a Low Dimensional Manifold Model. arXiv:1803.07252.
- Zhao, H.; Jiang, L.; Jia, J.; Torr, P.; and Koltun, V. 2021. Point Transformer. arXiv:2012.09164.